Ultrasensitive gas detection of large-area boron-doped graphene

Ruitao Lv[a,b,c,1], Gugang Chen[d,1], Qing Li[e,1], Amber McCreary[b,c,1], Andrés Botello-Méndez[f,1], S. V. Morozov[g], Liangbo Liang[h], Xavier Declerck[f], Nestor Perea-López[b,c], David A. Cullen[i], Simin Feng[b,c], Ana Laura Elías[b,c], Rodolfo Cruz-Silva[j], Kazunori Fujisawa[b,c], Morinobu Endo[j], Feiyu Kang[a], Jean-Christophe Charlier[f], Vincent Meunier[h], Minghu Pan[k], Avetik R. Harutyunyan[d], Konstantin S. Novoselov[g], and Mauricio Terrones[b,c,j,l,m,2]

[a]Key Laboratory of Advanced Materials of Ministry of Education of China, School of Materials Science and Engineering, Tsinghua University, Beijing, 100084, China; [b]Department of Physics, The Pennsylvania State University, University Park, PA 16802; [c]Center for 2-Dimensional and Layered Materials, The Pennsylvania State University, University Park, PA 16802; [d]Honda Research Institute USA Inc., Columbus, OH 43212; [e]Institute of Functional Nano and Soft Materials and Collaborative Innovation Center of Suzhou Science and Technology, Soochow University, Jiangsu 215123, China; [f]Institute of Condensed Matter and Nanosciences, Université catholique de Louvain, 1348 Louvain-la-Neuve, Belgium; [g]School of Physics & Astronomy, University of Manchester, Manchester, M13 9PL, United Kingdom; [h]Department of Physics, Applied Physics and Astronomy, Rensselaer Polytechnic Institute, Troy, NY 12180; [i]Materials Science & Technology Division, Oak Ridge National Laboratory, Oak Ridge, TN 37831; [j]Research Center for Exotic Nanocarbons, Shinshu University, Wakasato 4-17-1, Nagano 380-8553, Japan; [k]School of Physics, Huazhong University of Science and Technology, Wuhan 430074, China; [l]Department of Chemistry, The Pennsylvania State University, University Park, PA 16802; and [m]Department of Materials Science & Engineering, The Pennsylvania State University, University Park, PA 16802

Heteroatom doping is an efficient way to modify the chemical and electronic properties of graphene. In particular, boron doping is expected to induce a *p*-type (boron)-conducting behavior to pristine (nondoped) graphene, which could lead to diverse applications. However, the experimental progress on atomic scale visualization and sensing properties of large-area boron-doped graphene (BG) sheets is still very scarce. This work describes the controlled growth of centimeter size, high-crystallinity BG sheets. Scanning tunneling microscopy and spectroscopy are used to visualize the atomic structure and the local density of states around boron dopants. It is confirmed that BG behaves as a *p*-type conductor and a unique croissant-like feature is frequently observed within the BG lattice, which is caused by the presence of boron-carbon trimers embedded within the hexagonal lattice. More interestingly, it is demonstrated for the first time that BG exhibits unique sensing capabilities when detecting toxic gases, such as NO_2 and NH_3, being able to detect extremely low concentrations (e.g., parts per trillion, parts per billion). This work envisions that other attractive applications could now be explored based on as-synthesized BG.

graphene | boron-doped | STM | gas sensor | B-C trimers

G raphene is a fascinating material that has created an unprecedented impact in condensed-matter physics, chemistry, materials science, and industry (1–6). According to theory, the valence and conduction bands of pristine (nondoped) graphene (PG) touch at the *K* point in the Brillouin zone, thus making it behave as a zero-overlap semimetal (7). This lack of band gap limits graphene applications in some areas including semiconductor electronics. Therefore, it is crucial to tailor the electronic properties of graphene and eventually be able to open an electronic band gap. Doping, especially chemical doping, constitutes an efficient way to modify the electronic, chemical, and magnetic properties of materials. Recently, exciting progress has been achieved regarding graphene chemical doping, and more detailed information can be found in the literature (8, 9). Among different dopants, the two most adjacent neighbors of carbon in the periodic table of the elements (i.e., B and N) have attracted the attention of numerous scientists because of their similar atomic sizes with C and potential to induce *p*-type (boron) and *n*-type (nitrogen) conduction in graphene. In particular, the synthesis of N-doped graphene (NG) (10–14), as well as its atomic scale characterization (15–18) and possible applications (19–21), have been well explored. However, experimental progress on boron-doped graphene (BG) (22–27) is still very scarce compared with that on NG. Actually, theoretical work on BG has been extensively carried out to demonstrate the properties of BG and its possible applications, including field-effect transistors

(FETs) (28), hydrogen storage (29), and Li-ion batteries (LIBs) (30). In particular, density functional theory (DFT) calculations predicted that FETs fabricated with BG could exhibit high ON/OFF ratios and low subthreshold swings (28). Moreover, B atoms embedded within the graphene lattice can lead to improved hydrogen storage capacity by decreasing the H_2 adsorption energy dramatically (29). Compared with PG, more Li ions could be captured around boron-doping sites in BG because of the formation of an electron-deficient structure. In this context, Yakobson et al. have demonstrated that the substitutional doping of boron in graphene could lead to much improved Li storage performance with small volume variation during discharge/charge cycles and a capacity of 857 mAh/g (as $Li_{1.5}C_3B$), which is two times higher than that of graphite (372 mAh/g) (30). Besides that, it has been theoretically demonstrated that BG could break the symmetry of spin-up and spin-down transmittance channel, thus leading to a metallic-to-semiconductor transition. In this sense, it is believed that BG

Significance

The gas-sensing performance of graphene could be remarkably enhanced by incorporating dopants into its lattice based on theoretical calculations. However, to date, experimental progress on boron-doped graphene (BG) is still very scarce. Here, we achieved the controlled growth of large-area, high-crystallinity BG sheets and shed light on their electronic features associated with boron dopants at the atomic scale. As a proof-of-concept, it is demonstrated that boron doping in graphene could lead to a much enhanced sensitivity when detecting toxic gases (e.g. NO_2). Our results will open up new avenues for developing high-performance sensors able to detect trace amount of molecules. In addition, other new fascinating properties can be exploited based on as-synthesized large-area BG sheets.
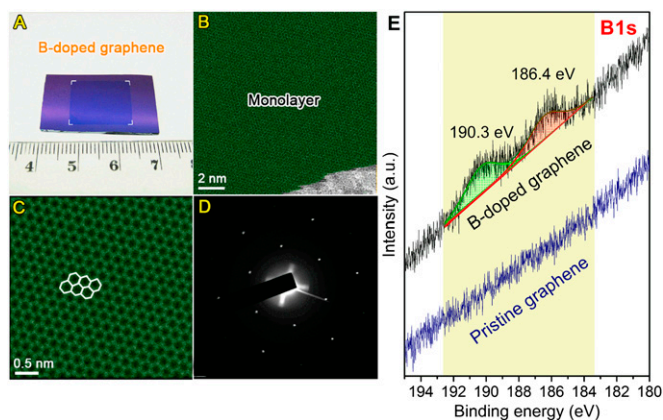
ENGINEERING

Fig. 1. Morphology of BG sheets. (*A*) Photograph of BG sheet (1.6 cm × 1.2 cm) transferred onto SiO₂/Si substrate. (*B* and *C*) Aberration-corrected medium-angle annular dark-field STEM images of BG sheets. The monolayer region is shown in green. (*D*) SAED pattern depicting the hexagonal characteristic of the doped graphene lattice. Both *C* and *D* show that the hexagonal lattice of graphene is not perturbed even with substitutional boron doping. (*E*) XPS B1s fine scan of BG and PG samples.

could become a good candidate for developing spin filter devices. Moreover, from the theoretical standpoint, it has been recently demonstrated that the sensitivity and selectivity of graphene-based gas sensors could be remarkably enhanced by incorporating dopants or defects within the graphene lattice (31). These results open up the possibility of constructing excellent graphene-based sensors to efficiently detect flammable and toxic gases.

To experimentally confirm some of the above-mentioned theoretical predictions, it is important to be able to synthesize large-area, highly crystalline BG in a controllable and reproducible way. Furthermore, it is very important to visualize how B atoms bond to C atoms within the sp^2 hybridized carbon layer to understand the electronic and chemical properties of BG. The present work describes the controlled growth of large-area (~cm²), high-crystallinity BG sheets grown on copper foils by bubbler-assisted chemical vapor deposition (BA-CVD) at atmospheric pressure. Scanning tunneling microscopy/spectroscopy (STM/STS) was used to understand the electronic features associated with boron dopants at the atomic scale. Characteristic croissant-like (or boomerang-like) features within the BG samples were observed via STM, which are very

different from the single substitutional B-dopants observed in BG samples synthesized by low-pressure CVD (LP-CVD) routes (23). These features can be attributed to a vacancy-substitution complex involving three quasiadjacent B atoms. This was confirmed by comparing the experimental STM and STS data with corresponding simulations using state-of-the-art first-principles calculations. As a proof-of-concept, it is demonstrated, for the first time to our knowledge, that boron doping in graphene could lead to an enhanced sensitivity when detecting toxic gases, such as NO_2 and NH_3. It is foreseen that the large-area BG sheets described here could result in novel electronic or magnetic properties not reported hitherto.

Results and Discussion

BG synthesis and transfer procedures are described in *SI Appendix, SI Text* and Figs. S1–S3. In general, for CVD growth of nanostructures, the type of precursor and substrate are key prerequisites. In this work, a triethylborane (TEB)/hexane solution and copper foil (99.8% purity, 25 µm thick; Alfa Aesar) were used as the precursor and substrate, respectively. Compared with highly toxic precursors [e.g., diborane B_2H_6 (23, 32)] or solid precursors [e.g., boron powder (27)], TEB/hexane solutions appear to be safer and relatively easy to handle during BG synthesis. Moreover, by controlling the ratio of TEB and hexane, it is also possible to tune up the boron-doping concentration in BG. Regarding the substrate, Cu foil has proven to be an excellent choice for growing PG monolayers (33). By etching the Cu away, large-area BG sheets can be easily transferred onto different substrates (e.g., SiO₂/Si wafers or quartz slides as shown in *SI Appendix, Fig. S3* and Fig.1*A*). It should be mentioned that the sizes and shapes of the final BG sheets are only restricted by those of the original Cu foils used for transfer. By tailoring the shape of poly(methyl methacrylate)-coated BG/Cu foils, it is demonstrated that the letters "PSU" composed of BG sheets can be obtained (*SI Appendix, Fig. S3B*). Although it is very hard to obtain gram-scale monolayer material compared with other methods [e.g., solvothermal growth (34), chemical exfoliation of natural graphite (35)], CVD still has some obvious advantages. For example, it is possible to synthesize large-area BG monolayers with specific size and shape from CVD-grown samples. Furthermore, as-synthesized large-area BG samples are preferable for the assembly of electronic devices and to perform atomic-scale characterization such as STM/STS.

To evaluate the monolayer percentage of as-synthesized BG sheets, atomic force microscopy (AFM) was used to characterize the height profile of BG on SiO₂/Si substrate. A typical AFM image can be found in *SI Appendix, Fig. S4*. Based on AFM analysis, more than 90% of the measured area consisted of monolayer BG with heights less than 1.0 nm. Fig. 1*B* shows a representative aberration-corrected
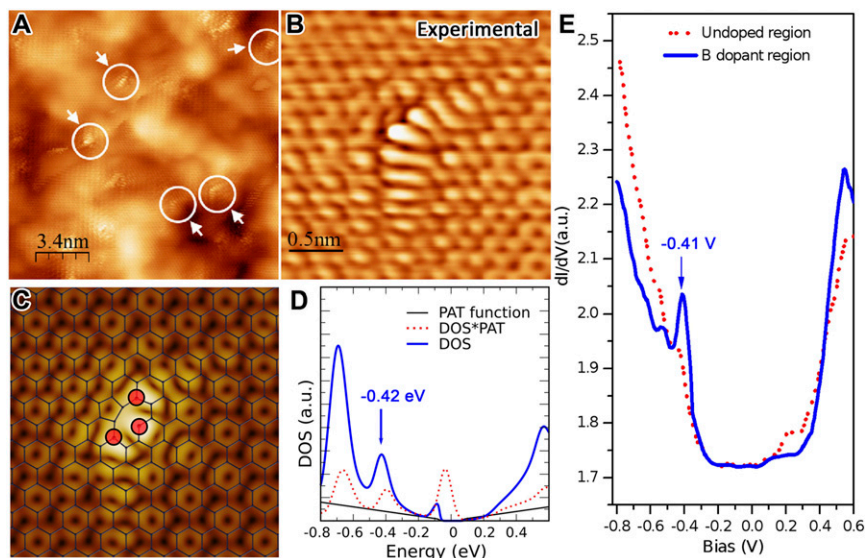
Fig. 2. Atomic-scale structure of boron dopants in as-synthesized BG sheets. (*A*) Large-area STM image of the BG illustrating the presence of numerous B dopants with similar croissant-like configuration (highlighted by white arrows). (*B*) Highly resolved experimental STM image of a croissant-like feature. (*C*) Simulated STM image and corresponding ball–stick structural model of B₃ dopant. (*D*) Simulated STS of the B₃-doping region shown in *C*. (*E*) dI/dV curves measured on B₃ dopants (blue solid curve) and on nondoped graphene region (red dot curve).

Fig. 3. Raman analysis of as-transferred BG sheets on SiO_2/Si substrate. (*A*) Typical Raman spectra of PG (nondoped) and BG sheets. The Raman laser line is 514 nm. (*B*) D-peak over G-peak intensity ratio (I_D/I_G) mapping of BG. (*C*) Position distributions of G peak and (*D*) Two-dimensional peak with the corresponding I_D/I_G ratios of BG sheets.
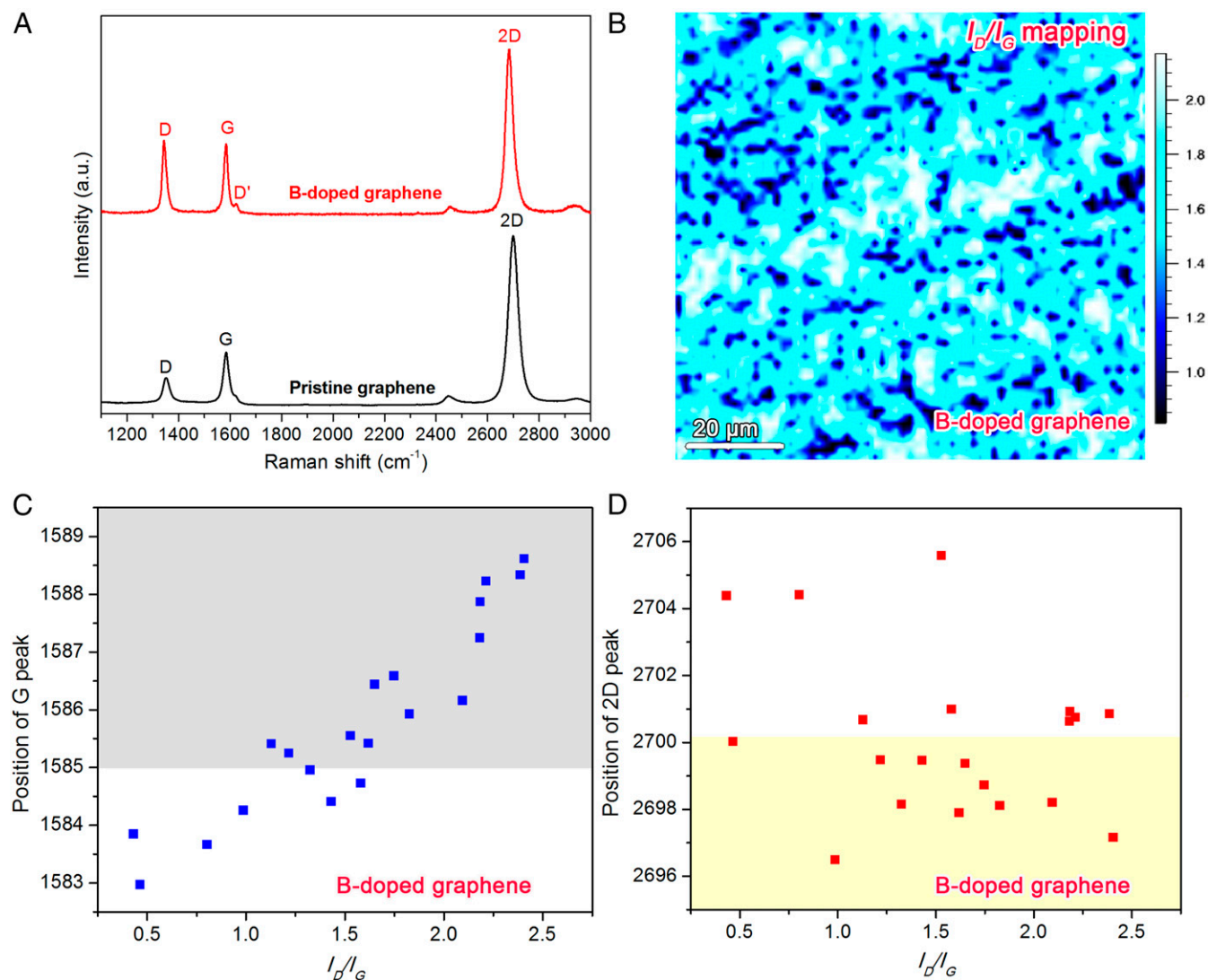
scanning transmission electron microscope (STEM) image of as-synthesized BG sheets. The monolayer region is shown in green. Based on both STEM and AFM measurements, it can be confirmed that the synthetic strategy can remarkably promote the growth of monolayer BG sheets. Furthermore, the size of as-synthesized BG is just determined by that of the Cu foil substrates considering the conformal coverage of BG. In addition, the aberration-corrected STEM image (Fig. 1*C*) and selected-area electron diffraction (SAED) pattern (Fig. 1*D*) of BG sheets clearly display the hexagonal lattice of graphene. The grain sizes of PG and as-synthesized BG sheets were analyzed by dark-field transmission electron microscopy (DF-TEM) observation, as shown in *SI Appendix*, Figs. S5–S7. DF-TEM images revealed that both PG and BG are composed of grains ranging from ~100 nm to over 1 μm (*SI Appendix*, Figs. S5 and S6). According to low-magnification DF-TEM image from BG (*SI Appendix*, Fig. S7), ~7 μm of large domain was observed. X-ray photoelectron spectroscopy (XPS) and STM/STS studies were performed to confirm the presence of B and to clearly identify B atoms within the lattice (see below). The XPS survey scan of freshly synthesized BG samples on copper foil substrates is shown in *SI Appendix*, Fig. S8*A*. The B-doping level in the as-synthesized BG sample is ~1.75 atomic % (more details can be found in the *SI Appendix*). The C1s fine-scan results of BG and PG sample are

shown in *SI Appendix*, Fig. S8 *B* and *C*, respectively. No obvious difference of C1s spectra can be found in these two samples, except for a small increase in the full-width at half maximum (FWHM) of the peaks. However, from the B1s spectra shown Fig. 1*E*, one can clearly see the difference between BG and PG samples. In the case of PG, no B signal in the B1s line scans can be detected (Fig. 1*E*). For BG, two prominent peaks located at approximately 186.4 and 190.3 eV are identified in the B1s line scans (Fig. 1*E*), which could be assigned to the substitutional boron atoms embedded within the graphene lattice and edge oxidized boron, respectively (36, 37).

The electronic and chemical properties of doped graphene highly depend on the atomic details of how the foreign atoms incorporate into the honeycomb lattice. Indeed, for the case of nitrogen-doped graphene, the local electronic properties can change dramatically depending on how nitrogen binds to the host crystal (18). Therefore, atomic characterization is mandatory. Fig. 2*A* illustrates the characteristic STM topography of the synthesized BG samples. The peculiar feature detailed in Fig. 2*B* is consistently observed throughout the sample. Considering the length scale and its symmetry, it is inferred that the defect should be more complex than a simple B substitution. *Ab initio* STM simulations provide several candidates with the same symmetry (*SI Appendix*, Fig. S9); however, to unambiguously identify the defect, a comparison of
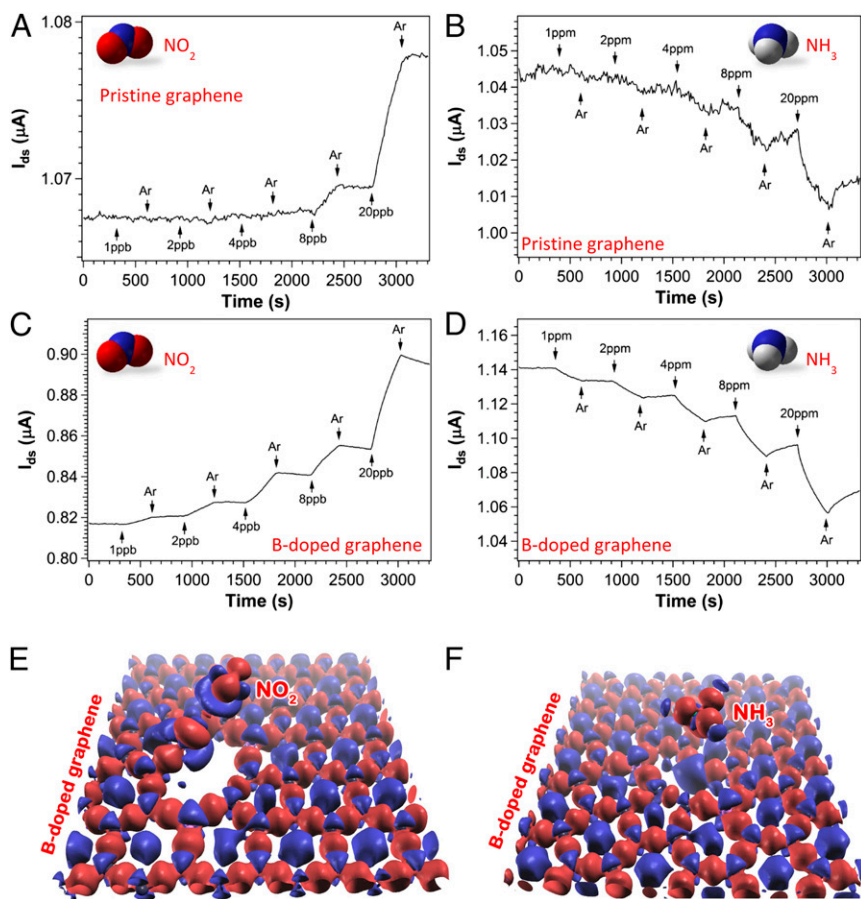
Fig. 4. Comparison of sensor response between PG (nondoped) and BG sheets. (*A* and *B*) Sensor response of PG sheets versus time recorded with the sensor exposed to NO_2 (*A*) and NH_3 (*B*). (*C* and *D*) Corresponding gas sensing on BG sheets when the sensor was exposed to NO_2 (*C*) and NH_3 (*D*). All experiments were carried out under in situ UV light illumination. Successive experiments were done after the device had been recovered. *E* and *F* demonstrate the difference of charge density with respect to the isolated atoms for the B_3-doped graphene with NO_2 and NH_3 molecules, respectively.

the STS should also be carried out. Figs. 2*C* and 3*D* exhibit the simulated STM and STS of the candidate that best matches the experimental observations. The effect of phonon-assisted tunneling (PAT) has been included in the simulation of the STS (38). The feature at −0.42 eV is consistent with the experimental STS measurement depicted in Fig. 2*E*. Therefore, although the comparison is not perfect, the defect is attributed to the geometry shown in Fig. 2*C*. The discrepancies might arise from the Tersoff–Hamann approximation (i.e., the effect of the shape of the tip might be more important than expected) and from interaction with the substrate.

Raman spectroscopy is a powerful technique for characterizing doping in graphene-like materials. The typical Raman spectra of as-synthesized BG and PG are shown in Fig. 3*A*. An enhanced D-band and a prominent D′-band can be observed in BG compared with bands characteristic of PG. It is well known that the D-band of graphene is caused by the breathing modes of six-atom rings and a defect is necessary for its activation. The D′-band could be attributed to a double resonance occurring by an intravalley process (39). The D-peak intensity (I_D) over the G-peak intensity (I_G) mapping is shown in Fig. 3*B*. The significant intensity of the D-band in BG could be attributed to the presence of defects caused by in-plane doping of B atoms embedded within the graphene hexagonal lattice. Furthermore, B doping will modify the Fermi surface of graphene and lead to a shift of the Raman peak positions. Previous work has demonstrated that the G-band will upshift for both hole and electron doping. In this study, B is expected to induce hole doping in graphene and a dominant upshift can be seen in the G-band of BG (Fig. 3*C*), which is in agreement with the hole doping by applying a gate voltage (40). However, the 2D band (also known as G′-band) responds differently to holes and electron doping. In previous work on NG, a remarkable downshift (7 cm^{-1}) was reported in NG compared with that of PG (18). For BG, dominant downshifts and some upshifts can be monitored, as shown in Fig. 3*D*. Another obvious difference

between BG and PG is the I_{2D}/I_G ratio. From Fig. 3*A*, the I_{2D}/I_G ratio of BG is lower than that of PG. From the mapping results shown in *SI Appendix*, Fig. S10, some parts of the BG sheets show I_{2D}/I_G ratio less than 2 (see dark blue parts in *SI Appendix*, Fig. S10). This is in agreement with the AFM studies which demonstrated that some multilayer regions coexist with monolayer graphene in BG samples.

To investigate the effect of B doping on graphene's gas sensitivity, comparative studies on NO_2 and NH_3 under similar detection environment were carried out. It is known that the interaction between adsorbed molecules and graphene will alter the electronic structure of graphenes as reflected by the change of current. The sensing experiments were carried out at a fixed drain to source voltage (V_{ds}) of 10- and 1-mV under continuous in situ UV light illumination for BG and PG sensors, respectively. The results are shown in Fig. 4 *A–D*. For NO_2 detection, PG cannot detect any obvious signal until the NO_2 concentration reaches 8 ppb, where a signal-to-noise ratio (s/n) of 9.4 is registered. In comparison, a clean signal with s/n = 31.5 at 1 ppb of NO_2 exposure to BG was observed. The same kind of improvement has been observed for NH_3 detection (e.g., PG can detect 20 ppm of NH_3 with s/n = 9.5, whereas B-doped graphene can easily sense 1 ppm with s/n = 50.1). Assuming a linear extrapolation, the sensitivity can be defined as the signal-to-noise ratio divided by gas concentration at the lowest tested concentration, such that B doping of graphene has enhanced its sensitivity 27 and 105 times to reach detection limits of 95 and 60 ppb (s/n = 3), respectively, for NO_2 and NH_3 detections.

Compared with typical sensing performance of graphene-based devices reported in the literature (Table 1), the CVD grown graphene sensors presented here, both with and without B doping, have very high sensitivities. Note that the current experiments were performed under continuous in situ UV light illumination. As reported previously (41, 42), UV light induced molecular desorption that dynamically keeps the sensor surface fresh, and UV light is believed to contribute to the overall sensor performance. Because PG and

Table 1. Typical performance of graphene based gas sensors

Target gas	Sensing material	Lowest concentration tested	Detection limit
NO_2	Mechanically exfoliated graphene (46)	100 ppm	—
	CVD graphene-like films (47)	65 ppm	—
	Ozone-treated graphene (48)	200 ppm	1.3 ppb
	Ethylenediamine-modified rGO (49)	1 ppm	70 ppb
	Sulfonated rGO (49)	5 ppm	3.6 ppm
	Epitaxial graphene from SiC (50)	2.5 ppm	—
	MPECVD graphene (51)	100 ppm	—
	rGO (52)	5 ppm	—
	rGO (53)	2 ppm	—
	Carbon Nanotubes/rGO hybrid (54)	0.5 ppm	—
	Mechanically exfoliated graphene (55)	1 ppm	The order of 1 ppb
	CVD graphene (56)	100 ppb	100 ppb
	CVD graphene (present work)	8 ppb	2.6 ppb
	B-doped CVD graphene (present work)	1 ppb	95.2 ppt
NH_3	rGO (52)	5 ppm	—
	Mechanically exfoliated graphene (55)	1 ppm	—
	CVD graphene (57)	65 ppm	—
	rGO/polyaniline hybrid (58)	5 ppm	—
	Mechanically exfoliated graphene (59)	10 ppm	—
	rGO (60)	20 ppm	—
	CVD graphene (58)	500 ppb	500 ppb
	rGO (61)	10,000 ppm (1%)	—
	rGO (53)	10,000 ppm (1%)	—
	CVD graphene (present work)	20 ppm	6.3 ppm
	B-doped CVD graphene (present work)	1 ppm	59.9 ppb

MPECVD, microwave plasma enhanced CVD; rGO, reduced graphene oxide. Dashes indicated that no data are available.

BG samples were grown under the same controlled environment except for the precursor, it was assumed that the relative enhancement of sensitivity after B doping is attributable to stronger molecule and graphene interaction, which could bring a larger conductivity change upon gas exposure. Based on first-principles calculations, Dai et al. (43) predicted that B-doped and S-doped graphene were able to chemically bind NO_2 and therefore dramatically increase their sensitivities to NO_2 molecules. Zhang et al. (31) simulated the interactions between small gas molecules (CO, NO, NO_2, and NH_3) and various graphene sheets including pristine, B-, or N-doped and defective graphenes. The authors' calculation demonstrates that all four gas molecules show much stronger adsorption on the doped or defective graphenes than that on the PG. Stronger adsorption or interaction between gas molecules and graphene is certainly beneficial for sensor applications. The experiments presented here agree very well with those theoretical predictions (31, 43). The present work clearly illustrates that the sensitivity of graphene-based sensors could indeed be significantly enhanced by introducing dopants such as boron into the graphene sheets. Charge and population analysis reveal that B_3-doped graphene exhibits enhanced sensing compared with PG because B_3-doped graphene reveals a larger affinity to both donor and acceptor molecules, such as NH_3 and NO_2 (Fig. 4 *E* and *F* and the *SI Appendix*).

In summary, large-area and high-quality BG sheets were synthesized by using a liquid precursor of TEB/hexane solution. Unique croissant-like features corresponding to B_3-dopants embedded within the hexagonal BG lattice are visualized for the first time to our knowledge with STM/STS techniques. As-synthesized BG can be applied to detect gas molecules at extremely low concentrations with a clean signal of s/n = 31.5 for 1 ppb NO_2 exposure and s/n = 50.1 for 1 ppm NH_3. Compared with PG, B doping of graphene can significantly enhance the sensitivity 27 and 105 times for NO_2 and NH_3 detections, respectively. Our results will open up new avenues for developing high-performance sensors able to detect trace amount of molecules. In addition, other new fascinating properties can be exploited based on the controllable synthesis of high-quality BG sheets.

Methods

Synthesis of BG Sheets. The synthesis of large-area BG was achieved using a BA-CVD system, which can be seen in *SI Appendix,* Fig. S1. A typical run for BG synthesis can be described as follows. Firstly, copper foils (99.8% purity, 25 μm thick; Alfa Aesar) were cleaned in a diluted HCl aqueous solution (HCl:H_2O = 1:3 vol/vol), dried with N_2, and then loaded into the quartz tubing reactor. After degassing, the reactor was heated up to 1,000 °C with the steps shown in *SI Appendix*, Fig. S2 and kept constant for 10 min to anneal the copper foils. Then, a TEB/hexane solution was bubbled with 1 sccm Ar into the reactor at 1,000 °C for 5 min. Finally, the reactor was cooled to room temperature in an Ar flow. The copper foils with BG sheets were taken out of the reactor for further characterizations. PG sheets were synthesized using only hexane as precursor. More details about BG transfer, XPS, and Raman characterization can be found in the *SI Appendix*.

STM/STS Measurements and DFT Simulation. STM measurements were conducted with a home-built variable temperature STM in an ultrahigh vacuum (UHV) system with a base pressure better than 1×10^{-10} millibars. The BG samples were degassed in UHV at ~200 °C for several hours before performing the STM/STS measurements. In this study, all of the STM/STS data were acquired at 85 K if not otherwise stated. The bias voltage was applied on the sample during the STM observations. STM simulations were carried out within the Tersoff–Hamann approach (44) from DFT using a localized numerical basis set and norm-conserving pseudopotentials as implemented in the SIESTA package (45). Spin-polarized calculations were carried out to verify whether the systems exhibit a magnetic moment. STS was simulated from the projected density of states around the center of the defect. More details can be found in the *SI Appendix*.

Device Fabrication. A 5-mm-by-5-mm graphene piece was transferred onto a *p*-type Si substrate for device fabrication, where the Si has an oxide thickness around 300 nm. Two circular (diameter, 3 mm) electrical contacts made up of Au/Ti in the thicknesses of 120 nm/30 nm were applied 3 mm apart on top of graphene through vacuum thermal deposition.

Gas Sensing Measurements. Details regarding the device fabrication and electrical conductance measurements can be found in previous work (41, 42). In the present case, certified 1 ppm (1,000 ppm) mixture gas of NO_2 (NH_3) in Ar was used for dilution, where the concentration was confirmed by chemiluminescence measurement (gravimetric method). Research-grade (99.9999% purity) Ar was used as the carrier gas. A total flow rate of 1,000 mL/min was used for all experiments. To

ENGINEERING

minimize experimental errors, gas dilution was restricted to a simple one-step mixing of carrier and analyte gases controlled by two digital mass flow controllers (MFCs) (model no. 5850S; Brooks). Both MFCs were calibrated using a multipoint calibration curve with gas measurement equipment (DHI) accurate to 0.01 mL/min. The flow accuracy of these MFCs is ± 0.7% of flow rate and ± 0.2% of full scale. Based on these specifications and the gas flow rates used, the gas concentration error after dilution is estimated to be no more than 20% for the detection range used in this study. Two electrical contacts (Au/Ti with thicknesses of 120 nm/30 nm) were applied on top of the graphene through vacuum thermal deposition. Gas sensing measurements were done on a customized flowing cell that has electrical feedthrough connections for temperature and electrical measurements. The current was monitored with a Keithley 4200-SCS instrument at atmospheric pressure and a fixed room temperature of 25 °C through a temperature controller equipped with automatic heating and cooling assemblies. In situ UV light (λ = 253.7 nm and I of ~1.7 mW/cm^2) was applied through a quartz window onto the device for all gas detection experiments.

1. Novoselov KS, et al. (2004) Electric field effect in atomically thin carbon films. *Science* 306(5696):666–669.

2. Zhang Y, et al. (2009) Direct observation of a widely tunable bandgap in bilayer graphene. *Nature* 459(7248):820–823.

3. Lin YM, et al. (2011) Wafer-scale graphene integrated circuit. *Science* 332(6035):1294–1297.

4. Yang X, Cheng C, Wang Y, Qiu L, Li D (2013) Liquid-mediated dense integration of graphene materials for compact capacitive energy storage. *Science* 341(6145):534–537.

5. Tassin P, Koschny T, Soukoulis CM (2013) Applied physics. Graphene for terahertz applications. *Science* 341(6146):620–621.

6. Reich ES (2013) Graphene knock-offs probe ultrafast electronics. *Nature* 497(7450):422–423.

7. Castro Neto AH, Guinea F, Peres NMR, Novoselov KS, Geim AK (2009) The electronic properties of graphene. *Rev Mod Phys* 81(1):109–162.

8. Terrones H, Lv R, Terrones M, Dresselhaus MS (2012) The role of defects and doping in 2D graphene sheets and 1D nanoribbons. *Rep Prog Phys* 75(6):062501.

9. Lv RT, Terrones M (2012) Towards new graphene materials: Doped graphene sheets and nanoribbons. *Mater Lett* 78:209–218.

10. Wei D, et al. (2009) Synthesis of N-doped graphene by chemical vapor deposition and its electrical properties. *Nano Lett* 9(5):1752–1758.

11. Guo B, et al. (2010) Controllable N-doping of graphene. *Nano Lett* 10(12):4975–4980.

12. Sun Z, et al. (2010) Growth of graphene from solid carbon sources. *Nature* 468(7323):549–552.

13. Zhang C, et al. (2011) Synthesis of nitrogen-doped graphene using embedded carbon and nitrogen sources. *Adv Mater* 23(8):1020–1024.

14. Jin Z, Yao J, Kittrell C, Tour JM (2011) Large-scale growth and characterizations of nitrogen-doped monolayer graphene sheets. *ACS Nano* 5(5):4112–4117.

15. Meyer JC, et al. (2011) Experimental analysis of charge redistribution due to chemical bonding by high-resolution transmission electron microscopy. *Nat Mater* 10(3):209–215.

16. Zhao L, et al. (2011) Visualizing individual nitrogen dopants in monolayer graphene. *Science* 333(6045):999–1003.

17. Deng DH, et al. (2011) Toward N-Doped Graphene via Solvothermal Synthesis. *Chem Mater* 23(5):1188–1193.

18. Lv R, et al. (2012) Nitrogen-doped graphene: Beyond single substitution and enhanced molecular sensing. *Sci Rep* 2:586.

19. Wang X, et al. (2009) N-doping of graphene through electrothermal reactions with ammonia. *Science* 324(5928):768–771.

20. Qu L, Liu Y, Baek JB, Dai L (2010) Nitrogen-doped graphene as efficient metal-free electrocatalyst for oxygen reduction in fuel cells. *ACS Nano* 4(3):1321–1326.

21. Reddy ALM, et al. (2010) Synthesis of nitrogen-doped graphene films for lithium battery application. *ACS Nano* 4(11):6337–6342.

22. Zhu QQ, Yu JH, Zhang WS, Dong HZ, Dong LF (2013) Solvothermal synthesis of boron-doped graphene and nitrogen-doped graphene and their electrical properties. *J Renew Sustain Energy* 5(2):021408.

23. Zhao L, et al. (2013) Local atomic and electronic structure of boron chemical doping in monolayer graphene. *Nano Lett* 13(10):4659–4665.

24. Wang H, et al. (2013) Synthesis of boron-doped graphene monolayers using the sole solid feedstock by chemical vapor deposition. *Small* 9(8):1316–1320.

25. Gebhardt J, et al. (2013) Growth and electronic structure of boron-doped graphene. *Phys Rev B* 87(15):155437.

26. Sheng ZH, Gao HL, Bao WJ, Wang FB, Xia XH (2012) Synthesis of boron doped graphene for oxygen reduction reaction in fuel cells. *J Mater Chem* 22(2):390–395.

27. Li X, et al. (2012) Boron Doping of Graphene for Graphene-Silicon p-n Junction Solar Cells. *Adv Energy Mater* 2(4):425–429.

28. Huang B (2011) Electronic properties of boron and nitrogen doped graphene nanoribbons and its application for graphene electronics. *Phys Lett A* 375(4):845–848.

29. Zhou YG, Zu XT, Gao F, Nie JL, Xiao HY (2009) Adsorption of hydrogen on boron-doped graphene: A first-principles prediction. *J Appl Phys* 105(1):014309.

30. Liu Y, Artyukhov VI, Liu M, Harutyunyan AR, Yakobson BI (2013) Feasibility of Lithium Storage on Graphene and Its Derivatives. *J Phys Chem Lett* 4(10):1737–1742.

31. Zhang YH, et al. (2009) Improving gas sensing properties of graphene by introducing dopants and defects: A first-principles study. *Nanotechnology* 20(18):185504.

32. Panchokarla LS, et al. (2009) Synthesis, Structure, and Properties of Boron- and Nitrogen-Doped Graphene. *Adv Mater* 21(46):4726–4730.

33. Li X, et al. (2009) Large-area synthesis of high-quality and uniform graphene films on copper foils. *Science* 324(5932):1312–1314.

34. Lin TQ, Huang FQ, Liang J, Wang YX (2011) A facile preparation route for boron-doped graphene, and its CdTe solar cell application. *Energy Environ Sci* 4(3):862–865.

35. Wu ZS, Ren W, Xu L, Li F, Cheng HM (2011) Doped graphene sheets as anode materials with superhigh rate and large capacity for lithium ion batteries. *ACS Nano* 5(7):5463–5471.

36. Shirasaki T, Derre A, Menetrier M, Tressaud A, Flandrois S (2000) Synthesis and characterization of boron-substituted carbons. *Carbon* 38(10):1461–1467.

37. Kim YA, et al. (2012) Raman spectroscopy of boron-doped single-layer graphene. *ACS Nano* 6(7):6293–6300.

38. Zhang YB, et al. (2008) Giant phonon-induced conductance in scanning tunnelling spectroscopy of gate-tunable graphene. *Nat Phys* 4(8):627–630.

39. Ferrari AC, Basko DM (2013) Raman spectroscopy as a versatile tool for studying the properties of graphene. *Nat Nanotechnol* 8(4):235–246.

40. Das A, et al. (2008) Monitoring dopants by Raman scattering in an electrochemically top-gated graphene transistor. *Nat Nanotechnol* 3(4):210–215.

41. Chen G, Paronyan TM, Harutyunyan AR (2012) Sub-ppt gas detection with pristine graphene. *Appl Phys Lett* 101(5):053119.

42. Chen G, Paronyan TM, Pigos EM, Harutyunyan AR (2012) Enhanced gas sensing in pristine carbon nanotubes under continuous ultraviolet light illumination. *Sci Rep* 2:343.

43. Dai JY, Yuan JM, Giannozzi P (2009) Gas adsorption on graphene doped with B, N, Al, and S: A theoretical study. *Appl Phys Lett* 95(23):232103.

44. Tersoff J, Hamann DR (1985) Theory of the scanning tunneling microscope. *Phys Rev B Condens Matter* 31(2):805–813.

45. Soler JM, et al. (2002) The SIESTA method for ab initio order-N materials simulation. *J Phys Condens Matter* 14(11):2745–2779.

46. Ko G, et al. (2010) Graphene-based nitrogen dioxide gas sensors. *Curr Appl Phys* 10(4):1002–1004.

47. Samsonau SV, Shvarkov SD, Meinerzhagen F, Wieck AD, Zaitsev AM (2013) Growth of graphene-like films for NO$_2$ detection. *Sens Actuators B Chem* 182:66–70.

48. Chung MG, et al. (2012) Highly sensitive NO$_2$ gas sensor based on ozone treated graphene. *Sens Actuators B Chem* 166:172–176.

49. Yuan W, Liu A, Huang L, Li C, Shi G (2013) High-performance NO$_2$ sensors based on chemically modified graphene. *Adv Mater* 25(5):766–771.

50. Pearce R, et al. (2011) Epitaxially grown graphene based gas sensors for ultra sensitive NO$_2$ detection. *Sens Actuators B Chem* 155(2):451–455.

51. Joshi RK, Gomez H, Alvi F, Kumar A (2010) Graphene Films and Ribbons for Sensing of O$_2$, and 100 ppm of CO and NO$_2$ in Practical Conditions. *J Phys Chem C* 114(14):6610–6613.

52. Fowler JD, et al. (2009) Practical chemical sensors from chemically derived graphene. *ACS Nano* 3(2):301–306.

53. Lu G, Ocola LE, Chen J (2009) Reduced graphene oxide for room-temperature gas sensors. *Nanotechnology* 20(44):445502.

54. Jeong HY, et al. (2010) Flexible room-temperature NO$_2$ gas sensors based on carbon nanotubes/reduced graphene hybrid films. *Appl Phys Lett* 96(21):213105.

55. Schedin F, et al. (2007) Detection of individual gas molecules adsorbed on graphene. *Nat Mater* 6(9):652–655.

56. Yavari F, Castillo E, Gullapalli H, Ajayan PM, Koratkar N (2012) High sensitivity detection of NO2 and NH3 in air using chemical vapor deposition grown graphene. *Appl Phys Lett* 100(20):203120.

57. Gautam M, Jayatissa AH (2011) Gas sensing properties of graphene synthesized by chemical vapor deposition. *Mater Sci Eng C* 31(7):1405–1411.

58. Huang XL, et al. (2012) Reduced graphene oxide-polyaniline hybrid: Preparation, characterization and its applications for ammonia gas sensing. *J Mater Chem* 22(42):22488–22495.

59. Dan Y, Lu Y, Kybert NJ, Luo Z, Johnson ATC (2009) Intrinsic response of graphene vapor sensors. *Nano Lett* 9(4):1472–1475.

60. Huang XL, et al. (2013) The NH$_3$ sensing properties of gas sensors based on aniline reduced graphene oxide. *Synth Met* 185:25–30.

61. Lu G, Yu K, Ocola LE, Chen J (2011) Ultrafast room temperature NH$_3$ sensing with positively gated reduced graphene oxide field-effect transistors. *Chem Commun (Camb)* 47(27):7761–7763.